Available online at www.sciencedirect.com
ScienceDirect
Trans. Nonferrous Met. Soc. China 27(2017) 1026−1035
Transactions of Nonferrous Metals Society of China
www.tnmsc.cn

Microstructure evolution during heat treatment of Mg−Gd−Y−Zn−Zr alloy and its low-cycle fatigue behavior at 573 K

Luo-yi WU[1,2], Hao-tian LI[1], Zhong YANG[3]

1. College of Materials Science and Engineering, Hunan University, Changsha 410082, China;
2. Hunan Province Key Laboratory for Spray Deposition Technology and Application, Hunan University, Changsha 410082, China;
3. College of Materials Science and Engineering, Xi'an Technological University, Xi'an 710032, China

Received 28 January 2016; accepted 18 January 2017

Abstract: In as-cast Mg−2.1Gd−1.1Y−0.82Zn−0.11Zr (mole fraction, %) alloy, lamellar microstructures that extend from grain boundaries to the interior of α-Mg grains are identified as clusters of γ' using a scanning transmission electron microscope equipped with a high-angle annular dark-field detector. Under a total strain-controlled low-cyclic loading at 573 K, the mechanical response and failure mechanism of Mg−2.1Gd−1.1Y−0.82Zn−0.11Zr alloy (T6 peak-aging heat treatment) were investigated. Results show that the alloy exhibits cyclic softening response at diverse total strain amplitudes and 573 K. The experimental observations using scanning electron microscopy show that the micro-cracks initiate preferentially at the interface between long-period stacking order structures and α-Mg matrix and extend along the basal plane of α-Mg. The massive long-period stacking order structures distributed at grain boundaries impede the transgranular propagation of cracks.

Key words: Mg−Gd−Y−Zn−Zr alloy; long-period stacking order structure; low-cycle fatigue at high temperature; crack initiation and propagation

1 Introduction

Mg−rare earth (RE) alloys have been widely available and applied as high-performance lightweight structural materials. These alloys included Mg−Nd, Mg−Y−Nd, Mg−Th and Mg−Ag−Nd for long-life service at high temperatures of 448 to 573 K [1−3]. It was reported that simultaneous additions of gadolinium and yttrium resulted in high strength at high temperature and good corrosion resistance [4]. Mg−Gd−Y−Zr alloy is generally fabricated by sand-casting [5−7], die casting [8,9] and semi-continuous casting [10], etc. The newly developed Mg−Gd−Y−Zr alloys showed considerable precipitation hardening [11], and its strength, elongation and creep resistance are superior to those of commercial WE54 and WE43 alloys [12,13].

Zn addition into binary Mg−Gd [14,15], Mg−Y [16,17] and ternary Mg−Gd−Y [18−20] systems resulted in long-period stacking order (LPSO) structure formation and improved mechanical properties. The composition, structure, and properties of Mg−RE(Gd, Y)−Zn alloys with LPSO structures have been extensively studied [21−26]. Industrial application of Mg−RE(Gd,Y) alloy systems requires knowledge of the mechanical response and failure behavior of both monotonic tensile loading and cyclic deformation. WANG et al [27] investigated the cyclic mechanical response of extruded Mg−Gd−Y magnesium alloy at room temperature. JANIK et al [28] and WU et al [29] reported the elevated-temperature fatigue behavior of peak-aged Mg−Gd−Y−Zr alloy. As potential structure materials used at 573 K, the Mg−Gd−Y−Zn−Zr alloys certainly experience alternate loading at elevated- temperature during their service life. Considering the LPSO distributions in the Mg−Gd−Y−Zn−Zr alloy, the fatigue behavior could be different from that of the Zn-free alloys.

This study aimed to: 1) explore the mechanical response of Mg−2.1Gd−1.1Y−0.82Zn−0.11Zr alloy under cyclic loading at high temperature; 2) understand

Foundation item: Project (2015TP1035) supported by the Science and Technology Planning Project of Hunan Province, China; Project (531107040183) supported by the Fundamental Research Funds for the Central Universities, China
Corresponding author: Luo-yi WU; Tel/Fax: +86-731-88823920; E-mail: wuluoyi@hnu.edu.cn
DOI: 10.1016/S1003-6326(17)60120-1

the role of LPSO in this investigated alloy under cyclic loading at 573 K and 3) elucidate the failure mechanisms of the alloy under the combined action of high temperature and cyclic stress.

2 Experimental

2.1 Materials

Mg−Gd−Y−Zn−Zr alloy was prepared referring to YANG et al [30]. Practical chemical composition of the alloy analyzed by inductively coupled plasma spectrometer (ICP) is Mg−11.80Gd−3.42Y−1.91Zn−0.35Zr (mass fraction, %) or Mg−2.1Gd−1.1Y−0.82Zn−0.11Zr (mole fraction, %). Note that mole fraction is used for the alloy compositions unless otherwise specified in this study.

2.2 Experimental procedure

After solution treatment for 12 h at 773 K, the as-cast ingot was then quenched into hot water of ~343 K, and aging treatment was subsequently conducted at 498 K to peak hardness (T6 tempers). Hardness tests were performed using Vickers hardness tester Wolpert 401MVA with 4.9 N load for 15 s. X-ray diffraction (XRD) analysis on a Rigaku D/Max 2400 X-ray diffractometer operated at 250 mA, 40 kV with Cu K_α radiation was employed to preliminary phase identification. A common transmission electron microscope (TEM) Hitachi H800 and a scanning transmission electron microscope Tecnai G^2 F20 equipped with a high-angle annular dark-field detector (HAADF-STEM) were used to clarify the features of rich-RE precipitates. Foils for TEM investigations were ground to 75−100 μm thickness following twin-jet electropolished. A brief low-energy ion beam milling (GATAN 691 PIPS) was performed to improve surface quality.

Cylindrical dog-bone shaped samples in T6 tempers with 25 mm gauge length and 6 mm diameter were used in this fatigue testing. Before experiment, sample surfaces were hand-ground progressively parallel to the specimen axis with emery papers of 1000, 2000 and 5000 grit to remove surface irregularities created by machining process. Low-cycle fatigue tests were performed at (573±2) K on a computerized RDL−50 fatigue testing system equipped with a heating-furnace. Cyclic loading was performed under total axial strain controlled with a strain ratio of $R_\varepsilon=\varepsilon_{min}/\varepsilon_{max}=-1$. The frequency of cycling held constant at 0.25 Hz until specimen failure. Triangular waveform loadings were applied at total strain amplitudes $\Delta\varepsilon_t/2$ of 0.3%, 0.45%, 0.6%, 0.75% and 0.9%. A scanning electron microscope (SEM) FEI QUANTA 200 was used to identify the crack-initiation sites and propagation behavior in fatigue failure specimens.

3 Results and discussion

3.1 Microstructures of as-cast specimen

Figure 1(a) shows the typical microstructures of as-cast specimens. The addition of zirconium and zinc resulted in grain sizes reducing to 20−30 μm in as-cast alloy. Herringbone compounds (black arrow) were mainly distributed at the grain boundaries. According to Fig. 1(b), dominant herringbone compounds in the as-cast alloy were identified as Mg_3Gd.

Aside from Mg_3Gd phase distribution along the grain boundaries in the as-cast alloy, plenty of lamellar microstructures (white arrow) existed adjacent to the grain boundaries (Fig. 1(a)). The lamellar microstructures extended from the grain boundaries to the interior of α-Mg grains, but were scarce at the centre of the grains. They developed along diverse directions in the as-cast alloy but parallel with one another in individual grains. It can be inferred that there exists specific orientation relationship between the lamellar microstructures and the α-Mg matrix. HAADF-STEM was used to clarify the features of lamellar microstructures. The characteristic feature of the material probed by high-angle annular dark-field imaging was the atomic number Z. Generally, for a crystal with constant thickness, bright intensity features correspond directly to the atomic columns with high mean square atomic number (Z^2).

Plate-like microstructures could be readily distinguished from the α-Mg matrix in as-cast alloys by their contrast in HAADF-STEM images (Fig. 1(c)). The remarkably long precipitate plates with extraordinarily large aspect ratios were less than 1 nm in thickness and parallel to $\{0001\}_{\alpha\text{-Mg}}$. In contrast to α-Mg matrix, the precipitate plates were much brighter, which indicated enrichment of the large atomic number Gd, Y and Zn atoms. The precipitate plates appeared in pairs or clusters in the as-cast Mg−2.1Gd−1.1Y−0.82Zn−0.11Zr alloy. The lamellar microstructures observed in the SEM images (Fig. 1(a)) were believed as clusters of RE-rich precipitate plates.

In Fig. 1(d) (incident electron beam parallel to $[11\bar{2}0]_{\alpha\text{-Mg}}$), there exist two layers of bright spots, which correspond to two adjacent close-packed planes of $\{0001\}_{\alpha\text{-Mg}}$. The ⋯ABABABCACACA⋯ stacking sequence along $[0001]_{\alpha\text{-Mg}}$, as well as enrichment of Gd, Y and Zn atoms in the B and C layers, was believed as the principal characteristics of the plate-like microstructures. In addition, occupancy of Gd, Y and Zn atoms showed the exact matching with the B and C layers of α-Mg in the habit plane. Similar precipitate plates have been reported by NIE et al [31,32] in

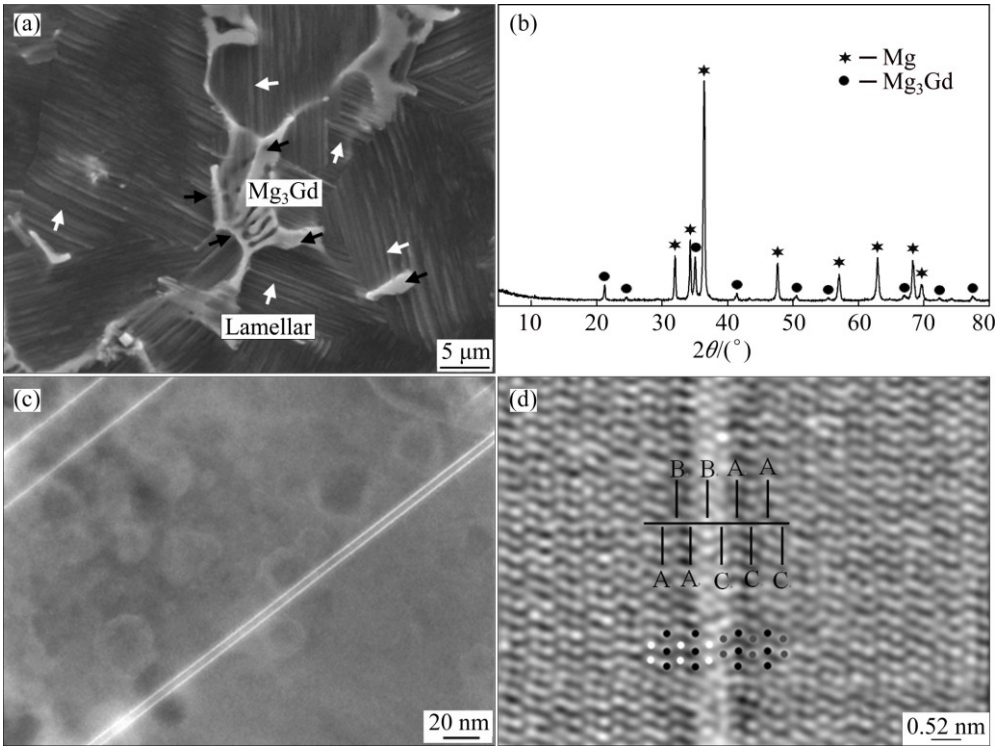

Fig. 1 Microstructures of as-cast Mg−2.1Gd−1.1Y−0.82Zn−0.11Zr alloy: (a) SEM image of second phase morphology and distribution; (b) X-ray diffraction pattern; (c) HAADF-STEM image of lamellar microstructures; (d) Fourier-filtered HAADF-STEM image of precipitate plates (Incident electron beam was parallel to $[11\bar{2}0]_{\alpha\text{-Mg}}$ in both (c) and (d))

over-aging Mg−1Gd−0.4Zn−0.2Zr (mole fraction, %) alloy, and named as γ' phase in response to precipitation sequence. In the present study, γ' phases were also detected in the as-cast Mg−2.1Gd−1.1Y−0.82Zn−0.11Zr alloy. Therefore, lamellar microstructures observed in the SEM images were believed as clusters of the γ' precipitate plates, which originated from the grain boundary second phases and extended into grain interior along $\{0001\}_{\alpha\text{-Mg}}$. It can be inferred that the high atomic number (Z) elements Zn, Gd and Y diffusion along the basal plane (close-packed plane) of α-Mg resulted in the lamellar microstructure formation during solidification.

3.2 Microstructures of solution-treated samples

Figure 2 shows the typical microstructures of solution-treated and water-quenched specimens. Herringbone structures (Fig. 1(a)) observed at the grain boundaries in the as-cast specimen were replaced by the blocky shape of the second phase after solution treatment. The second phase at the grain boundaries in the solution-treated sample became significantly wider than that in the as-cast specimen, from which it could be concluded that the volume fraction of second phase at the grain boundaries significantly increased after the solution treatment for 12 h at 773 K (Fig. 2(a)) compared with that of the as-cast specimen (Fig. 1(a)). In addition, the lamellar structures (Fig. 1(a)) were not detected in the solution-treated specimens (Fig. 2(a)), which is consistent with the experiment results reported by LI et al [33].

The phase compositions of the solution-treated sample were characterized by XRD and TEM. In Fig. 2(b), the second phase was identified as LPSO structures referring to Ref. [34]. TEM image of the solution-treated specimens is shown in Fig. 2(c). The incident electron beam was parallel to $[11\bar{2}0]_{\alpha\text{-Mg}}$. From the inserting diffraction pattern, there exist periodic small diffraction spots distributed at the interval of 1/14 of distance between the direct spot and the $(0002)_{\alpha\text{-Mg}}$ reflection. Therefore, these lamellae were identified as the 14H LPSO structures [19]. During solution heat treating at 773 K for 12 h, the high atomic number (Z) elements Zn, Gd and Y, which enriched in Mg_3(Gd, Y, Zn) phase, diffused along the basal plane (close-packed plane) into α-Mg matrix. Because of quite low diffusion velocity of the rare-earth elements in α-Mg, the Mg_3(Gd,Y,Zn) is hard to dissolve. As a result, the Mg_3Gd phase distributed at grain boundaries was substituted with stable LPSO structures after solution heat treatment.

3.3 Age-hardening characteristics and precipitation

The microhardness of the water-quenched specimens was approximately HV 79. The hardness initially increased slowly and then rapidly after 2 h aging. The hardness eventually reached peak at HV 107 after aging for 24 h and then gradually decreased. The

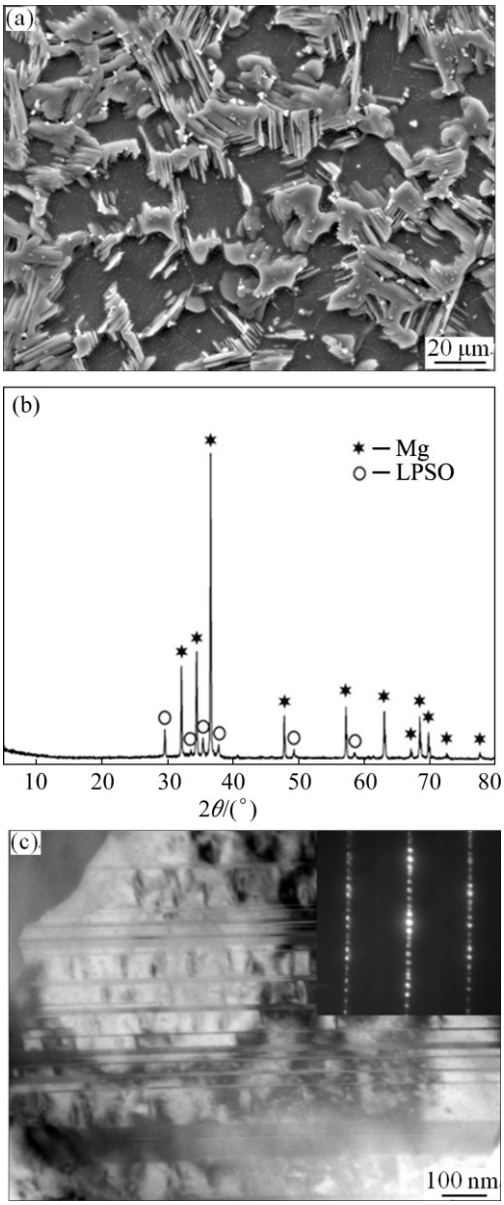

Fig. 2 Electron microscope images of solution-treated (773 K, 12 h) specimen of Mg−2.1Gd−1.1Y−0.82Zn−0.11Zr alloy: (a) SEM image showing second phase distribution; (b) X-ray diffraction pattern; (c) TEM image and corresponding electron diffraction pattern of second phase (incident electron beam B parallel to $[11\bar{2}0]_{\alpha\text{-Mg}}$)

hardness at peak-aged state increased by almost 36% (HV 28) compared with that of the as-quenched samples, which showed significant age-hardening response at 498 K. Figure 3 presents bright field TEM images and corresponding electron diffraction patterns of the peak-aged specimen.

Precipitates β' (indicated by black arrows) and β_1 (indicated by white arrows) were the key strengthening phases (Figs. 3(a) and (b)). Age hardening of the alloys occurred through sequential precipitations of β'', β' and β_1 phases [18,19]. The β_1 phase heterogeneously

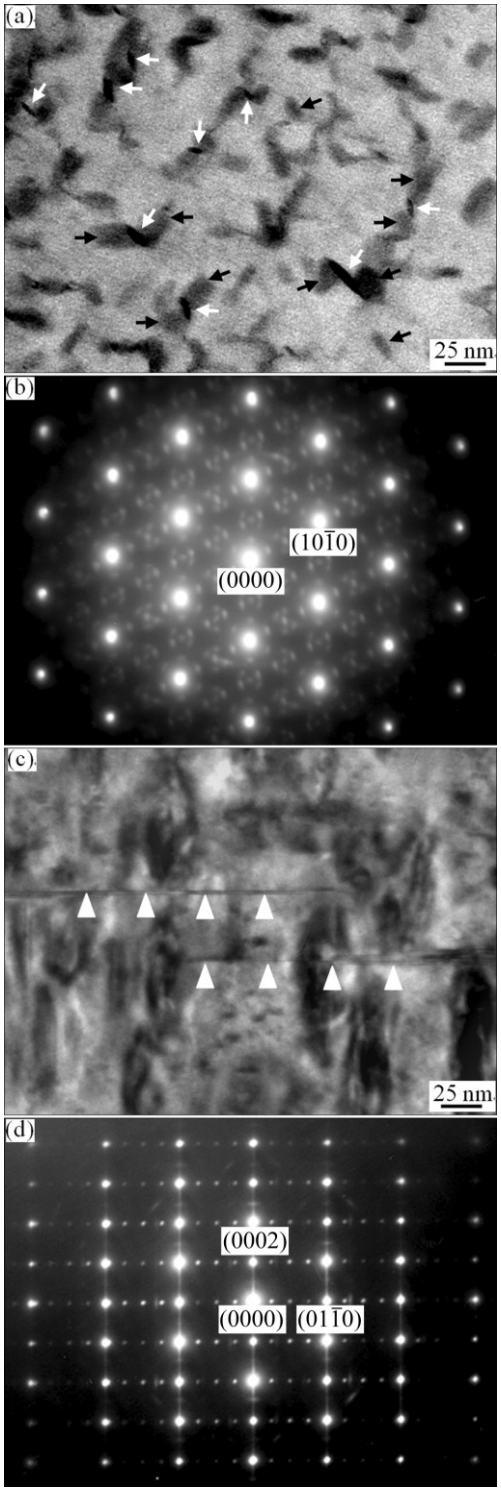

Fig. 3 TEM bright-field images (a, c) and corresponding selected area electron diffraction patterns (b, d) after sample was aged at 498 K for 24 h: (a, b) Incident electron beam B parallel to $[0001]_{\alpha\text{-Mg}}$; (c, d) B// $[11\bar{2}0]_{\alpha\text{-Mg}}$

nucleated at the interface of the β' phase and relaxed strain fields around the β' [18]. Plate-like precipitates were observed in the microstructure (Fig. 3(c), indicated by white triangle. These precipitates appeared as thin $(0001)_\alpha$ plates with several atom layers of thickness and

150 to 200 nm length, which were designated as γ'' phase [31,32]. The corresponding selected area electron diffraction pattern is shown in Fig. 3(d). Bright streaks along $[0001]_{\alpha\text{-Mg}}$ were detected, which were ascribed to the shape effects of the γ'' phase (precipitate plates).

3.4 Cyclic stress responses under total strain controlled tests at 573 K

Variations of the stress amplitudes with the number of loading cycles at 573 K for Mg−2.1Gd−1.1Y−0.82Zn−0.11Zr alloy in T6 tempers are shown in Fig. 4 on a semi-log scale. At high strain amplitudes (0.75% and 0.9%), the alloys showed apparent cyclic softening in whole cyclic life. As for the strain amplitudes of 0.3%, 0.45% and 0.6%, a slight cyclic softening feature was observed during the early cycles. The stress amplitudes remained almost constant during the half of the fatigue life, which showed pronounced cyclic saturation behavior at high temperature. In summary, as cyclic total strain amplitudes range from 0.3% to 0.9%, the alloy always exhibits cyclic softening at 573 K (Fig. 4).

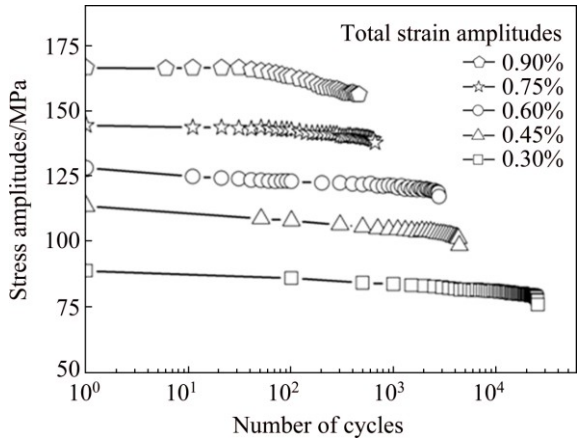

Fig. 4 Cyclic stress amplitude vs number of cycles at different total strain amplitudes of Mg−2.1Gd−1.1Y−0.82Zn−0.11Zr alloy in T6 temper

Cyclic hardening is a common phenomenon during fatigue tests, which arises from the interactions among the dislocations that impede their motion. As for the Mg−2.1Gd−1.1Y−0.82Zn−0.11Zr alloy in T6 temper, twinning, LPSO and precipitates besides dislocation–dislocation interactions can act as barriers to the dislocation movement and cause cyclic hardening. However, cyclic softening was detected during fatigue tests at 573 K (Fig. 4), which was entirely different from the cyclic hardening response at room temperature for Mg−8.0Gd−3.0Y−0.5Zr (mass fraction, %) [27], AZ31 [35,36] and AZ91 [37]. The first reason is that both dislocation slip and grain boundary sliding become propitious to operate as the temperature increased up to 573 K. Secondly, it was reported that dislocation nets, dislocation cells, sub-boundary structures as well as dynamic recrystallization grains were observed in the precipitation-free zone (PFZ) of the Mg−10Gd−2.0Y−0.46Zr (mass fraction, %) alloy after the cyclic loading under the 0.3% total strain amplitude at 573 K [29]. Therefore, it could be inferred that the dynamic recovery and recrystallization also exert an effect on the softening behavior for the Mg−2.1Gd−1.1Y−0.82Zn−0.11Zr alloy during cyclic loading at 573 K. In addition, the β' and β_1 precipitates, which were regarded as the key strengthening phases, also grew up gradually during fatigue tests at 573 K, thereby resulting in alloy over-aging. In summary, strength deterioration plays a key role in long-term cyclic loading. Therefore, the alloy generally exhibits cyclic softening response at 573 K.

Figure 5 shows the stress–strain hysteresis loops of the Mg−2.1Gd−1.1Y−0.82Zn−0.11Zr alloy in T6 temper obtained from fully reversed strain-controlled fatigue experiment at total strain amplitudes of 0.45%. The stress–strain hysteresis loops with respect to the loading cycles are plotted to clearly show the evolution of their shapes at total strain amplitudes of 0.45%. The tensile peak stresses clearly decreased during the entire fatigue life, but the compressive peak stresses after the half-life loading cycle until fatigue failure were practically unchanged. Macro-yielding is detectable from the hysteresis loop. Due to the small strain amplitude and the concave-down shape, dislocation slip was the major plastic deformation mechanism of the alloys at 573 K under cyclic loading at total strain amplitudes of 0.45%.

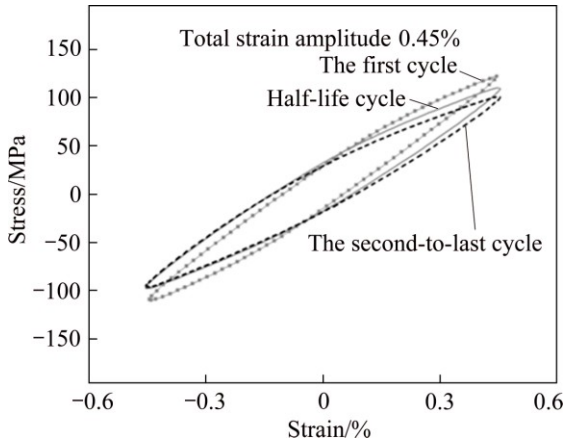

Fig. 5 Stress–strain hysteresis loops of different cycles at 0.45% total strain amplitudes

3.5 Micro-crack initiation and propagation behavior

Backscattered electron images (Fig. 6) showed the atomic number contrast near the main cracks of the failure sample of the Mg−2.1Gd−1.1Y−0.82Zn−0.11Zr alloy after cyclic test at 0.45% total strain amplitude. Backscattered electron images provided contrast based on differences in the average atomic number of different

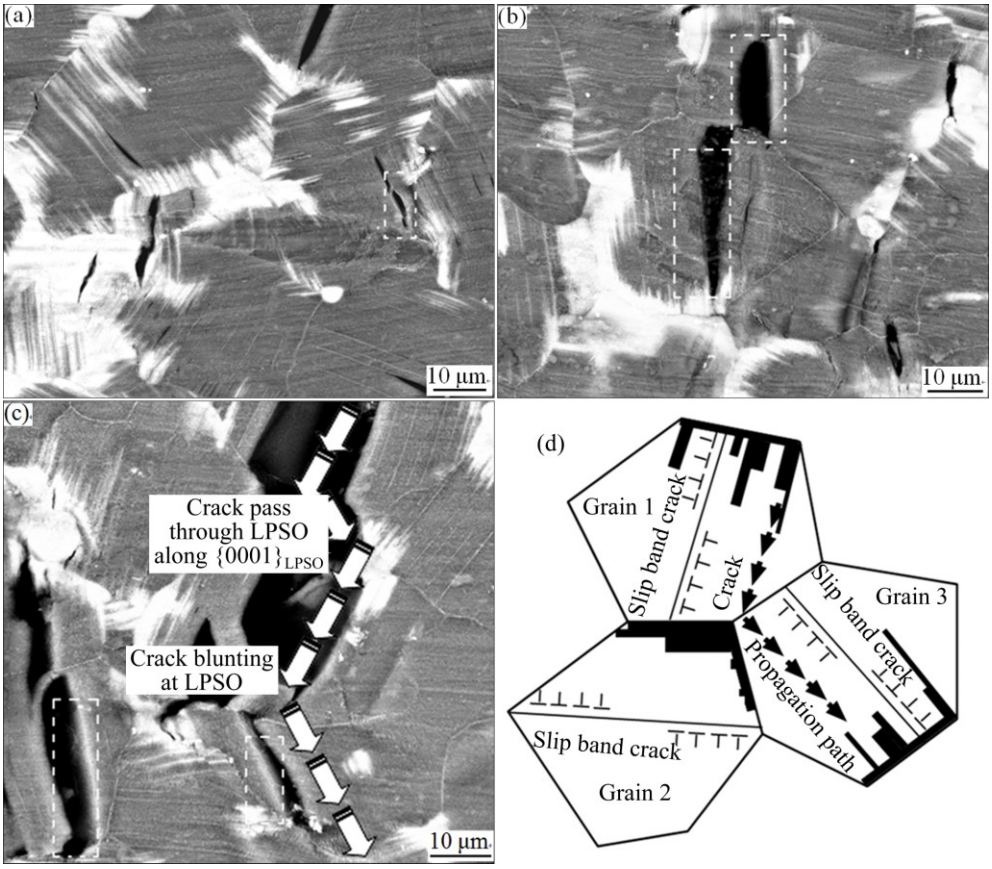

Fig. 6 Backscattered electron images of fatigue failure specimen near fracture under 0.45% total strain amplitude at 573 K: (a, b) Cracks initiation; (c) Cracks propagation behavior; (d) Schematic diagram showing cracks propagation

portions of the sample. The bright blocky phases represent the LPSO structures containing significant concentrations of high atomic number elements Gd, Y and Zn. The LPSO structures were extensively distributed at the grain boundaries and extended into the grain interiors along the $\{0001\}_{\alpha\text{-Mg}}$.

Micro-crack initiation generally occurred on the specimen surface (Figs. 6(a)−(c)) at the following sites: 1) interiors of the LPSO structures; 2) basal slip bands of $\{0001\}_{\alpha\text{-Mg}}$ and 3) interfaces between α-Mg and LPSO structures (marked by white dashed box). Experimental observations showed that the interfaces between α-Mg and LPSO structures were preferential sites for crack initiation. This finding was ascribed to different hardness between LPSO structures and α-Mg. The hardness of 18R-type LPSO structures is higher than that of α-Mg [23]. Thus, LPSO structures cannot exactly match the deformation of the α-Mg during cyclic loading. Therefore, the micro-cracks were preferentially initiated at the interfaces between the magnesium matrix and LPSO structures.

As the cracks grew into the small pieces of LPSO structures along the direction parallel to the $\{0001\}_{\text{LPSO}}$, the cracks passed through the LPSO and propagated into the adjacent grains as shown in Fig. 6(c). Crack blunting was observed when the cracks encountered the blocky LPSO structures at the grain boundaries, and the crack propagation direction remarkably deviated from the $\{0001\}_{\text{LPSO}}$ (Fig. 6(c)). As the cyclic test continued, micro-crack initiation occurred in other grains. The crack propagation resulted from merging of micro-cracks between adjacent grains. The crack propagation and change in direction are sketched in Fig. 6(d) when they encountered the blocky LPSO. The mechanism that LPSO structures hinder crack propagation is shown in Fig. 7. When micro-crack propagation encountered massive LPSO structures distributed at the grain boundaries, they usually tended to either generate cavities (Fig. 7(a)) or blunt (Fig. 7(b)) inside the LPSO structures. Nucleation of cavities at LPSO structures indicated that impingement of slip bands on LPSO resulted in stress concentration. Therefore, the shielding of a crack tip by LPSO at the grain boundaries impeded transgranular crack extension. Therefore, the blocky LPSO structures, particularly those distributed at the grain boundaries, acted as barriers to crack propagation.

Compared with the Mg−2.0Gd−0.60Y alloy, the addition of 0.82% Zn (mole fraction, %) into the investigated alloy resulted in the formation of LPSO structures. Given the LPSO structures in the

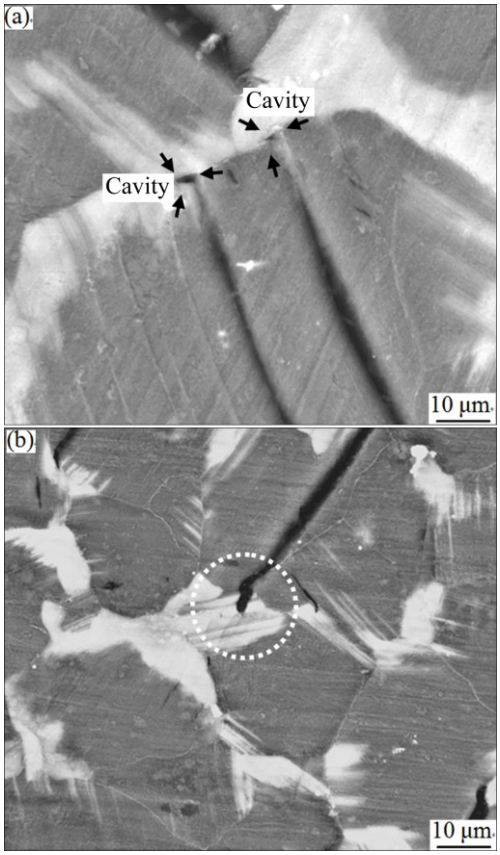

Fig. 7 Interaction between cracks and LPSO structures: (a) Micro-cracks generating cavities on LPSO structures; (b) Micro-cracks blunting inside LPSO structures

Mg−2.1Gd−1.1Y−0.82Zn−0.11Zr alloy, the initiation and propagation behavior of cracks at high temperature 573 K was significantly different from that in Zn-free alloy. With regard to Mg−2.0Gd−0.60Y alloy, micro-cracks initiated mostly either at grain boundaries for lower strain amplitudes or at the persistent slip bands for higher strain amplitudes, and then intercrystalline cracks propagated during the fatigue test at 573 K [29]. As for the Mg−2.1Gd−1.1Y−0.82Zn−0.11Zr alloy, the micro-cracks initiated mostly at the interfaces between the LPSO and the α-Mg, and then the mergers of micro-cracks between adjacent grains resulted in transgranular cracking. Therefore, transgranular cracking was recognized as the feature of fatigue failure at high temperature in the Mg−2.1Gd−1.1Y−0.82Zn−0.11Zr alloy.

Dense deformation twins were observed on the surface of fatigue failure specimen at 573 K (Fig. 8). FAN et al [38] also reported that a large number of twins existed near the fracture in an extruded magnesium alloy after cyclic deformation. It was believed that the distribution of the deformation twins depended on the strain amplitude, cyclic mechanical characteristics, and the plastic zone size ahead of the crack tip. Considering the basal slips as the key deformation mechanism below 623 K, the micro-cracks initiated at the $\{0001\}_{\alpha\text{-Mg}}$ slip bands. As thin twins were generated (Fig. 8), the micro-cracks no longer appeared as straight slits. When the micro-cracks propagated to the twins, deflection of propagation direction was observed. Twinning resulted in crack propagation along a winding route, which prolonged the extension distance.

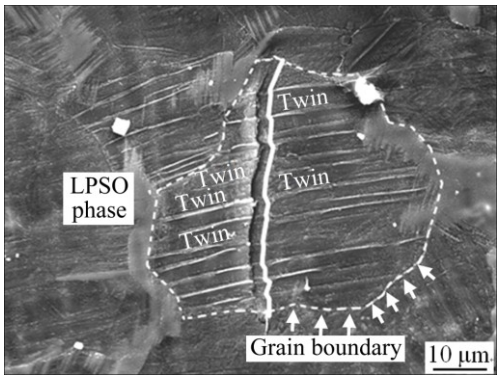

Fig. 8 Interaction between twins and micro-cracks

3.6 Fractography of fatigue failure

Fracture surfaces of fatigued specimens at the total strain amplitude of 0.45% were examined using SEM. The low-magnification image reflects the overall fracture morphology. A typical low-magnification SEM image of the fatigue crack initiation site and propagation zone of the specimens tested is presented in Fig. 9(a). Basically, the fatigue cracks initiated from the specimen surface. The fatigue fracture had a smooth appearance, and the specimens generally exhibited brittle fracture after the fatigue test. Radial marks were also observed on the macrograph, which indicated the direction of fracture at the final failure stage. Cleavage-like facets were observed at the initiation sites (Fig. 9(b)). This finding corresponded to the cracks preferentially nucleated at the interfaces between the LPSO and α-Mg, as well as the basal slip bands (Figs. 6(a)–(c)). The area of the fatigue-crack propagation zone is indicated by the dashed line on the image. The propagation area contained some fatigue striation-like features (marked by white arrowheads in Fig. 9(c)) that were perpendicular to the crack propagation direction. Some secondary cracks, marked by black arrowheads, are visible in Figs. 9(c) and (d). Figure 9(d) shows the features of the fracture surfaces at the stage of final static failures. Shallow dimples are observed in Fig. 9(d), which are relatively different from that of crack initiation (Fig. 9(b)) and propagation (Fig. 9(c)). According to Figs. 9(b) and (d), as the fatigue cracks propagated into the sample interiors, the mechanism of crack initiation is different from that of the micro-cracks on the specimen surface. In summary, the fracture characteristics changed from cleavage

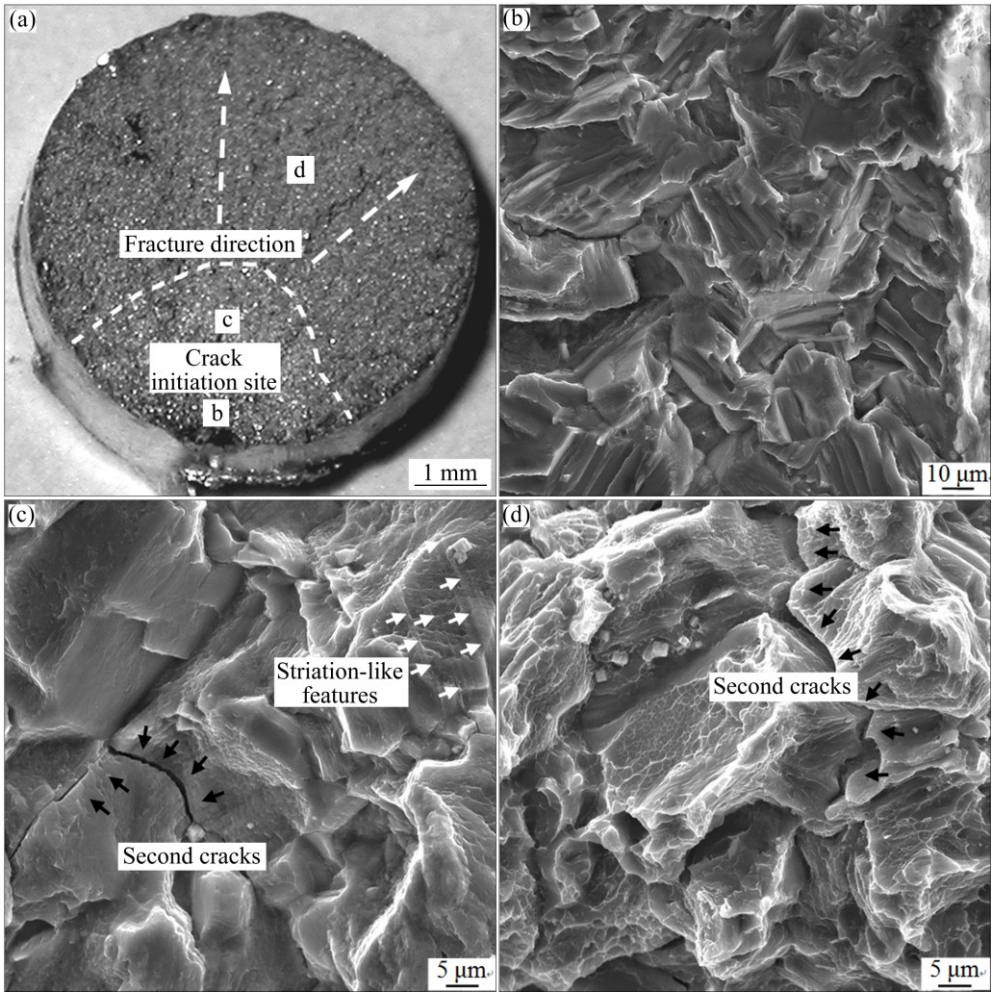

Fig. 9 Typical SEM images of fracture surfaces at total strain amplitudes of 0.45%

(Fig. 9(b)) to mixed mechanisms with a few shallow dimples distributed on the facets (Fig. 9(d)).

4 Conclusions

1) In the as-cast Mg−2.1Gd−1.1Y−0.82Zn−0.11Zr alloy, lamellar microstructures were identified as clusters of γ' precipitate plates. After 12 h solution heat treatment at 773 K, the clusters of γ' were dissolved into the α-Mg matrix and cannot be detected. When the alloy was aged to peak hardness at 498 K, the plate-like γ'' precipitates were distributed along $\{0001\}_{\alpha\text{-Mg}}$, which was one of the precipitation hardening phases.

2) Strain controlled low-cycle fatigue tests were performed on the Mg−2.1Gd−1.1Y−0.82Zn−0.11Zr alloy at 573 K. Cyclic softening responses were observed under diverse total strain amplitudes at 573 K. The interfaces between the LPSO structures and the α-Mg matrix are preferential sites for micro-crack initiation. The massive LPSO structures distributed at the grain boundaries impeded the transgranular propagation of micro-cracks. The merger of cracks in adjacent grains resulted in crack propagation.

3) Secondary crack nucleation preferentially occurred at the grain boundaries at the fatigue crack propagation and final static failures stages. Therefore, the fracture characteristics changed from cleavage to mixed mechanisms with a few shallow dimples distributed on the facets.

References

[1] MORDIKE B L. Development of highly creep resistant magnesium alloys [J]. Journal of Materials Processing Technology, 2001, 117(3): 391−394.

[2] MORDIKE B L. Creep-resistant magnesium alloys [J]. Materials Science and Engineering A, 2002, 324(1−2): 103−112.

[3] SMOLA B, STULÍOVÁ I, von BUCH F, MORDIKE B L. Structural aspects of high performance Mg alloys design [J]. Materials Science and Engineering A, 2002, 324(1−2): 113−117.

[4] NAKATSUGAWA I, KAMADO S, KOJIMA Y, NINOMIYA R, KUBOTA K. Corrosion of magnesium alloys containing rare earth elements [J]. Corrosion Reviews, 1998, 16(1−2): 139−158.

[5] MEI Jun, LIU Wen-cai, WU Guo-hua, ZHANG Yang, ZHANG Yi-tao, HONG Yi-kai, ZHANG Ruo-xi, XIAO Lu, DING Wen-jiang. Effect of complex melt-refining treatment on microstructure and mechanical properties of sand-cast Mg−10Gd−3Y−0.5Zr alloy [J].

Transactions of Nonferrous Metals Society of China, 2015, 25(6): 1811−1821.

[6] PANG Song, WU Guo-hua, LIU Wen-cai, ZHANG Liang, ZHANG Yang, CONRAD H, DING Wen-jiang. Influence of pouring temperature on solidification behavior, microstructure and mechanical properties of sand-cast Mg−10Gd−3Y−0.4Zr alloy [J]. Transactions of Nonferrous Metals Society of China, 2015, 25(2): 363−374.

[7] PANG Song, WU Guo-hua, LIU Wen-cai, ZHANG Liang, ZHANG Yang, CONRAD H, DING Wen-jiang. Influence of cooling rate on solidification behavior of sand-cast Mg−10Gd−3Y−0.4Zr alloy [J]. Transactions of Nonferrous Metals Society of China, 2014, 24(11): 3413−3420.

[8] WANG Zhi-qin, ZHANG Bin, LI De-jiang, FRITZSCH R, ZENG Xiao-qin, ROVEN H J, DING Wen-jiang. Effect of heat treatment on microstructures and mechanical properties of high vacuum die casting Mg−8Gd−3Y−0.4Zr magnesium alloy [J]. Transactions of Nonferrous Metals Society of China, 2014, 24(12): 3762−3768.

[9] LI Sheng-yong, LI De-jiang, ZENG Xiao-qin, DING Wen-jiang. Microstructure and mechanical properties of Mg−6Gd−3Y−0.5Zr alloy processed by high-vacuum die-casting [J]. Transactions of Nonferrous Metals Society of China, 2014, 24(12): 3769−3776.

[10] XU C, ZHENG M Y, CHI Y Q, CHEN X J, WU K, WANG E D, FAN G H, YANG P, Wang G J, LV X Y, XU S W, KAMADO S. Microstructure and mechanical properties of the Mg−Gd−Y−Zn−Zr alloy fabricated by semi-continuous casting [J]. Materials Science and Engineering A, 2014, 549: 128−135.

[11] CAO Liang, LIU Wen-cai, LI Zhong-quan, WU Guo-hua, XIAO Lu, WANG Shao-hua, DING Wen-jiang. Effect of heat treatment on microstructures and mechanical properties of sand-cast Mg−10Gd−3Y−0.5Zr magnesium alloy [J]. Transactions of Nonferrous Metals Society of China, 2014, 24(3): 611−618.

[12] ANYANWU I A, KAMADO S, KOJIMA Y. Aging characteristics and high temperature tensile properties of Mg−Gd−Y−Zr alloys [J]. Materials Transactions, 2001, 42(7): 1206−1211.

[13] ANYANWU I A, KAMADO S, KOJIMA Y. Creep properties of Mg−Gd−Y−Zr alloys [J]. Materials Transactions, 2001, 42(7): 1212−1218.

[14] YAMASAKI M, ANAN T, YOSHIMOTO S, KAWAMURA Y. Mechanical properties of warm-extruded Mg−Zn−Gd alloy with coherent 14H long periodic stacking ordered structure precipitate [J]. Scripta Materialia, 2005, 53(7): 799−803.

[15] YAMASAKI M, SASAKI M, NISHIJIMA M, HIRAGA K, KAWAMURA Y. Formation of 14H long period stacking ordered structure and profuse stacking faults in Mg−Zn−Gd alloys during isothermal aging at high temperature [J]. Acta Materialia, 2007, 55(20): 6798−6805.

[16] ZHU Y M, MORTON A J, WEYLAND M, NIE J F. Characterization of planar features in Mg−Y−Zn alloys [J]. Acta Materialia, 2010, 58(2): 464−475.

[17] SUZUKI M, KIMURA T, KOIKE J, MARUYAMA K. Strengthening effect of Zn in heat resistant Mg−Y−Zn solid solution alloys [J]. Scripta Materialia, 2003, 48(8): 997−1002.

[18] HONMA T, OHKUBO T, KAMADO S, HONO K. Effect of Zn additions on the age-hardening of Mg−2.0Gd−1.2Y−0.2Zr alloys [J]. Acta Materialia, 2007, 55(12): 4137−4150.

[19] YAMADA K, OKUBO Y, SHIONO M, WATANABE H, KOJIMA S K. Alloy development of high toughness Mg−Gd−Y−Zn−Zr alloys [J]. Materials Transactions, 2006, 47(4): 1066−1070.

[20] SHI Fei, WANG Chun-qing, ZHANG Zhong-ming. Microstructures, corrosion and mechanical properties of as-cast Mg−Zn−Y−(Gd) alloys [J]. Transactions of Nonferrous Metals Society of China, 2015, 25(7): 2172−2180.

[21] KAWAMURA Y, HAYASHI K, INOUE A, MASUMOTO T. Rapidly solidified powder metallurgy $Mg_{97}Zn_1Y_2$ alloys with excellent tensile yield strength above 600 MPa [J]. Materials Transactions, 2001, 42(7): 1172−1176.

[22] ABE E, KAWAMURA Y, HAYASHI K, INOUE A. Long-period ordered structure in a high-strength nanocrystalline Mg−1at% Zn−2at%Y alloy studied by atomic-resolution *Z*-contrast STEM [J]. Acta Materialia, 2002, 50(15): 3845−3857.

[23] ITOI T, SEIMIYA T, KAWAMURA Y, HIROHASHI M. Long period stacking structures observed in $Mg_{97}Zn_1Y_2$ alloy [J]. Scripta Materialia, 2004, 51(2): 107−111.

[24] MATSUDA M, II S, KAWAMURA Y, IKUHARA Y, NISHIDA M. Interaction between long period stacking order phase and deformation twin in rapidly solidified $Mg_{97}Zn_1Y_2$ alloy [J]. Materials Science and Engineering A, 2004, 386(1−2): 447−452.

[25] HU Mao-liang, WANG Qu-dong, JI Ze-sheng, XU Hong-yu, XIN Ming-de, MA Guo-rui. Wear behavior of Mg−10Y−4Gd−1.5Zn−0.4Zr alloy [J]. Transactions of Nonferrous Metals Society of China, 2016, 26(2): 406−413.

[26] HOMMA T, KUNITO N, KAMADO S. Fabrication of extraordinary high-strength magnesium alloy by hot extrusion [J]. Scripta Materialia, 2009, 61(6): 644−647.

[27] WANG Feng-hua, DONG Jie, JIANG Yan-yao, DING Wen-jiang. Cyclic deformation and fatigue of extruded Mg−Gd−Y magnesium alloy [J]. Materials Science and Engineering A, 2013, 561: 403−410.

[28] JANIK V, YIN D D, WANG Q D, HE S M, CHEN C J, CHEN Z, BOEHLERT C J. The elevated-temperature mechanical behavior of peak-aged Mg−10Gd−3Y−0.4Zr alloy [J]. Materials Science and Engineering A, 2011, 528(7−8): 3105−3112.

[29] WU L, YANG Z, XIA W, CHEN Z, YANG L. The cyclic softening and evolution of microstructures for Mg−10Gd−2.0Y−0.46Zr alloy under low cycle fatigue at 573 K [J]. Materials & Design, 2012, 36: 47−53.

[30] YANG Z, LI J P, GUO Y C, LIU T, XIA F, ZENG Z W, LIANG M X. Precipitation process and effect on mechanical properties of Mg−9Gd−3Y−0.6Zn−0.5Zr alloy [J]. Materials Science and Engineering A, 2007, 454−455: 274−280.

[31] NIE J F, GAO X, ZHU S M. Enhanced age hardening response and creep resistance of Mg−Gd alloys containing Zn [J]. Scripta Materialia, 2005, 53(9): 1049−1053.

[32] NIE J F, OH-ISHI K, GAO X, HONO K. Solute segregation and precipitation in a creep-resistant Mg−Gd−Zn alloy [J]. Acta Materialia, 2008, 56(20): 6061−6076.

[33] LI Meng, ZHANG Kui, DU Zhi-wei, LI Xing-gang, MA Ming-long. Microstructure evolution and mechanical properties of Mg−7Gd−3Y−1Nd−1Zn−0.5Zr alloy [J]. Transactions of Nonferrous Metals Society of China, 2016, 26(7): 1835−1842.

[34] PENG Qiu-ming, GUO Jian-xin, FU Hui, CAI Xue-cheng, WANG Ya-nan, LIU Bao-zhong, XU Zhi-gang. Degradation behavior of Mg-based biomaterials containing different long-period stacking ordered phases [J]. Scientific Reports, 2014, 4(1): 3620.

[35] BEGUM S, CHEN D L, XU S, LUO A A. Effect of strain ratio and strain rate on low cycle fatigue behavior of AZ31 wrought magnesium alloy [J]. Materials Science and Engineering A, 2009, 517(1−2): 334−343.

[36] BEGUM S, CHEN D L, XU S, LUO A A. Low cycle fatigue properties of an extruded AZ31 magnesium alloy [J]. International Journal of Fatigue, 2009, 31(4): 726−735.

[37] EISENMEIER G, HOLZWARTH B, HÖPPEL H W, MUGHRABI H. Cyclic deformation and fatigue behaviour of the magnesium alloy AZ91 [J]. Materials Science and Engineering A, 2001, 319−321: 578−582.

[38] FAN C L, CHEN D L, LUO A A. Dependence of the distribution of deformation twins on strain amplitudes in an extruded magnesium alloy after cyclic deformation [J]. Materials Science and Engineering A, 2009, 519(1−2): 38−45.

Mg−Gd−Y−Zn−Zr 合金在热处理中的组织演变和 573 K 下的低周疲劳行为

吴落义[1,2]，李浩田[1]，杨 忠[3]

1. 湖南大学 材料科学与工程学院，长沙 410082；
2. 湖南大学 喷射沉积湖南省重点实验室，长沙 410082；
3. 西安工业大学 材料科学与工程学院，西安 710032

摘 要：使用带有高角环形暗场探测器的扫描透射电镜研究了 Mg−2.1Gd−1.1Y−0.82Zn−0.11Zr 合金的铸态组织特征，确认了由晶界向晶内延伸的层片状结构为 γ′相的集合体；研究了时效峰值态的 Mg−2.1Gd−1.1Y−0.82Zn−0.11Zr 合金在总应变控制下的高温(573 K)低周疲劳测试中的力学响应和失效机制。在 573 K 下，合金在不同的总应变幅控制的循环加载中均表现出了循环软化的特征。扫描电镜的观察结果表明：微观裂纹优先在长周期有序相和基体的界面处形核，并沿基面扩展；分布于晶界处的、块状长周期有序相能抑制裂纹的穿晶扩展。

关键词：Mg−Gd−Y−Zn−Zr 合金；长周期有序相；高温低周疲劳；裂纹形核与扩展

(Edited by Yun-bin HE)